Sound Speed and Poisson's Ratio Calibration of (Split) Hopkinson Bar via Iterative Dispersion Correction of Elastic Wave

Hyunho Shin
Mechanics of Materials and Design Laboratory,
Department of Materials Engineering,
Gangneung-Wonju National University,
7 Jugheon-ghil,
Gangneung,
Gangwon-do 25457, South Korea
e-mail: hshin@gwnu.ac.kr

A process of calibrating a one-dimensional sound speed (c_o) and Poisson's ratio (ν) of a (split) Hopkinson bar is presented. This process consists of Fourier synthesis and iterative dispersion correction (time-domain phase shift) of the elastic pulse generated by the striker impact on a circular bar. At each iteration, a set of c_o and ν is assumed, and the sound speed versus frequency (c_{dc} versus f_{dc}) relationship under the assumed set is obtained using the Pochhammer–Chree equation solver developed herein for ground state excitation. Subsequently, each constituting wave of the overall elastic pulse is phase shifted (dispersion corrected) using the c_{dc}–f_{dc} relationship. The c_o and ν values of the bar are determined in the iteration process when the dispersion-corrected overall pulse profiles are reasonably consistent with the measured profiles at two travel distances in the bar. The observed consistency of the predicted (dispersion-corrected) wave profiles with the measured profiles is a mutually self-consistent verification of (i) the calibrated values of c_o and ν, and (ii) the combined theories of Fourier and Pochhammer–Chree. The contributions of the calibrated values of c_o and ν to contemporary bar technology are discussed, together with the physical significance of the tail part of a traveling wave according to the combined theories. A preprocessing template (in Excel®) and calibration platform (in MATLAB®) for the presented calibration process are openly available online in a public repository.
[DOI: 10.1115/1.4054107]

Keywords: elasticity, impact, mechanical properties of materials, vibration, wave propagation

1 Introduction

Precise calibration of the one-dimensional (1D) sound speed (c_o) and Poisson's ratio (ν) of a circular bar is essential in using the split Hopkinson bar (SHB) [1–16] and Hopkinson bar (HB) [17–31]. In the case of SHB experiments, the specimen properties are generally determined using the following equations [1–16]:

$$\sigma(t) = \left(\frac{A}{A_o}\right) E_o \varepsilon_T(t) \tag{1}$$

$$\dot{\varepsilon}(t) = -2\left(\frac{c_o}{L}\right) \varepsilon_R(t) \tag{2}$$

$$\varepsilon(t) = -2\left(\frac{c_o}{L}\right) \int_0^t \varepsilon_R(t)dt \tag{3}$$

where σ, ε, and $\dot{\varepsilon}$ are the nominal stress, nominal strain, and nominal strain rate of the specimen, respectively; ε_R is the reflected pulse strain recorded in the incident bar; ε_T is the transmitted pulse strain recorded in the transmitted bar; A and L denote the initial cross-sectional area and initial length of the specimen, respectively; A_o, E_o, and c_o denote the cross-sectional area, elastic modulus, and sound speed of the bar, respectively; t is the time. These notations are explained here (instead of in Nomenclature) as the above equations are unused in the dispersion correction (dc) process. According to Eq. (1), an accurate value of c_o is necessary for the precise measurement of specimen stress because E_o is given as $E_o = \rho c_o^2$, where ρ is the bar density. In Eqs. (2) and (3), an accurate value of c_o is also essential for accurate measurement of the strain rate and strain. When dispersion correction (dc) is applied to ε_I and ε_R, the necessity of precise calibration of both c_o and ν arises (which will be described below for the HB application). Therefore, for the accurate measurement of specimen properties using SHB, precise calibration of c_o and ν is fundamental.

In the case of the HB, the wave profiles at the impact-entering end surface of the bar are obtained via dispersion correction (dc) [17,–31] of the measured wave profile at the interim axial position of the bar, which necessitates a series of sound speeds at a range of frequencies. This sound speed (c_{dc}) versus frequency (f_{dc}) relationship, called the dispersion relationship, can be obtained by solving the Pochhammer–Chree equation (PCE) [18,32–41]. References [37,38] expressed the PCE in terms of the normalized frequency (F), normalized sound speed (C), and Poisson's ratio (ν). The solver in [37,38] subsequently solves the PCE first at arbitrary F values to obtain the (F, C) matrix by solely using the Poisson's ratio (ν) information. Then, it finally obtains the PCE solutions, i.e., (F_{dc}, C_{dc}) matrix, at exact F values ($F_{dc} = a f_{dc}/c_o$) necessary for dispersion correction (dc), which are determined using the information of the one-dimensional sound speed (c_o) and bar radius (a). Therefore, the precise calibration of c_o and ν for the HB and SHB is fundamental for the accurate measurement of a wave profile using HB (and SHB) via dispersion correction (dc).

Despite the importance of calibrating the properties (c_o and ν) of SHB and HB, only a few studies pursued precise calibration of them. For instance, Ref. [39] calibrated them using a limited number of frequencies involved in wave profile. However, the calibration based on a thorough dc that utilized all involved frequencies were rarely performed. Furthermore, to the best of the author's knowledge, the verification of predicted

Contributed by the Applied Mechanics Division of ASME for publication in the JOURNAL OF APPLIED MECHANICS. Manuscript received January 16, 2022; final manuscript received March 10, 2022; published online April 20, 2022. Assoc. Editor: Hareesh Tippur.

(dispersion-corrected) wave profiles at certain travel distances compared with measured profiles was also rare, which can occur only when the combined theories of Fourier and Pochhammer–Chree (PC) used in the dc are correct. Consequently, (i) this study presents a procedure and tool for the calibration of c_o and ν based on the iterative dc of an elastic wave using the combined theories. A preprocessing template (prepared in Excel®) and calibration platform (written in MATLAB®) are available online in a public repository [41]. Simultaneously, (ii) this study pursues the mutually self-consistent verification of the combined theories by demonstrating the coincidence of the predicted (dispersion-corrected) and measured wave profiles at two travel distances in a circular bar.

2 Literature Survey

2.1 Dispersion Correction in Bar Technology. HB [17–31] has traditionally been used to measure a transient pulse generated by the impact of a near-field blast or bullets. Conversely, SHB, which is also called the Kolsky bar [1–16], has been used extensively to measure dynamic material properties such as the stress–strain and strain rate–strain curves of versatile materials at strain rates of approximately 10^2–10^4 s^{-1}. These curves, together with the accurately extracted quasi-static material properties [42–44], are generally used to calibrate a strain rate-dependent constitutive model [45,46], which is indispensable for the simulation of the dynamic deformation behavior of solids and structures [47–54].

The shape of the elastic wave in SHB and HB distends with travel; this phenomenon is called dispersion. The physical origin of dispersion from the viewpoint of medium particle motion is inertia in the lateral motion associated with the axial disturbance. From the viewpoint of the wave propagation, a high-frequency wave component that constitutes the overall elastic wave is sluggish compared with the wave component with a lower frequency. The wave profile is generally measured at the interim axial position of the bar. In the case of HB, the front surface of the bar is the location of interest where an impact pulse enters the bar, whereas the specimen location is of interest in the case of SHB. Therefore, the measured wave profile in SHB and HB needs to be corrected to obtain the wave profiles at the locations of interest, which is a process called dc [18,27–30,55–66].

2.2 Combined Theories of Fourier and Pochhammer–Chree. Before performing dc, the measured wave profile at a certain position needs to be modeled mathematically using Fourier's theory in terms of a series of sinusoidal wave components with a range of frequencies; this process is called Fourier synthesis. Subsequently, the phase of each wave component of the Fourier-synthesized function is shifted to predict the overall wave profile at a given travel distance.

To shift the phases of the wave components that constitute the overall elastic pulse, a series of sound speeds over a range of frequencies must be known a priori. The c_{dc} versus f_{dc} relationship can be obtained by solving either the Rayleigh–Love equation (RLE) [23,67–69] or PCE [18,32–41]. The former (RLE) is the 1D wave equation with lateral inertia correction, whereas the latter (PCE) is the full 3D wave equation of motion that inherently accounts for lateral motion. The solutions (C versus F relationship) of both equations for a Poisson's ratio of 0.29 were well documented by Kolsky [70] and Graff [71], which illustrated the deviation of the RLE solution from the PCE counterpart as the frequency increased.

Thus, using PCE solutions predominantly for dc seems natural, as observed in previous studies [18,27–30,55–66]. Like any theory, the PC theory needs experimental verification. It was originally derived for *standing* waves in the bar extending from minus to plus infinity, which inherently considered up to an infinite wavelength ($a/\Lambda = 0$). Therefore, the applicability of PCE to *transient* waves in a bar of finite length with definite bar ends requires verification. Furthermore, the Fourier synthesis and phase shift of the elastic pulse recorded at discrete time points are performed under the premise of a finite time period with fundamental frequency, which introduces a limit in the wavelengths of the constituting waves ($\Lambda = c/f$). Therefore, the applicability of the combined theories of Fourier and PC to the dc of transient waves in SHB and HB requires verification.

2.3 Usage and Verification of the Combined Theories. As regards studies on SHB applications, idealized trapezoidal and/or rectangular pulses were often considered as the original (reference) pulse in Refs. [18,56,62,66] to predict the shape of traveled pulses at a given travel distance; the predicted wave profile could not be verified in essence because of the assumption of the idealized shapes as the original pulse. Wang and Li [65] obtained the dispersion-corrected signal at the specimen position without verification. In some studies [58,59,61], the dispersion-corrected profile after traveling a certain distance was compared with the measured profile, which demonstrated qualitative consistency. In the foregoing studies, information on the c_o and ν values and/or their determination method were unavailable, limiting the rigorous verification of the dispersion-corrected profile. In most studies on the dc of SHB signal [55–66], less fluctuating stress–strain curves of SHB specimens were demonstrated as a result of using unverified dispersion-corrected wave profiles.

In the study by Davies on the use of HB [18], the strain pulse generated by impact loading was shown to disperse with travel and develop oscillations in the plateau and tail of the traveling pulse. The periods of oscillations determined using a few oscillations were qualitatively consistent with the combined theory prediction with notable data scatter (Fig. 25 in Ref. [18]). Thenceforth, a number of studies have determined physical quantities (such as wave velocity and arrival time of waves) from a few oscillations based on visual inspection. In the case of Oliver [19], a few phase velocities and group velocities were determined from the wave oscillations and compared with PC theory-predicted velocity versus period curves; qualitative consistency was observed. Curtis et al. [20–22] interpreted the different types of oscillations to be caused by up to sixth-mode PC vibrations based on a qualitatively drawn frequency versus arrival time diagram. The qualitative consistencies of the wave velocities and arrival times in previous studies [18–22] essentially have limitations as a verification of the PC theory because the coincidence of the predicted wave profiles themselves with the experiment was unavailable.

Lee et al. [24,25] quantified the frequency versus arrival time map (an intensity map) via the Gaussian-windowed Fourier transform of the experimental wave profile in HB. Their intensity *map* was qualitatively consistent with the predicted *curve* based on the PC theory (Fig. 4 in Ref. [25]). They also compared the predicted values of the phase and group velocities with their experimental counterparts (Fig. 5 in Ref. [25]), which also showed a qualitative coincidence but with a notable discrepancy. Yew and Chen [26] presented the feasibility of the fast Fourier transform method in analyzing wave motion generated by striker impact based on the assumptions of material properties and waveform, which limited the verification of the PC theory. While Barr et al. [28] predicted the incident wave profiles to a HB under different assumptions using a rigorous treatment including magnitude correction [27,28,65], the predicted wave profiles themselves were compared without verification.

The most rigorous and clearest verification of the combined theories or their applicability may be the direct verification of the predicted (dispersion-corrected) wave profile with reference to the measured profile at a sufficiently traveled distance. As observed earlier and to the best of the author's knowledge, no direct verification of the applicability of the combined theories existed. As mentioned, only when both theories are correct, the predicted wave profile using them coincides with that of the experiment.

Two reasons may cause the unavailability of direct verification of the predicted (dispersion-corrected) wave profile. First, the

sound speed and Poisson's ratio of the bar could not be precisely calibrated because of the absence of an appropriate calibration tool. Therefore, in reality, the manufacturer-provided literature values of c_o and ν have been more readily available than the calibrated ones, although the determination method of the former has hardly been disclosed. As regards Poisson's ratio, its value was often assumed to be the values (e.g., 0.29 or 0.30) for which the PCE solutions were available in the existing studies [18,36], or the bar with such a manufacturer-provided value was selected.

The second cause may be the difficulty in obtaining PCE solutions specific to the researcher's bar with unique values of c_o, ν, and a. The PCE has an infinite number of solution branches and is cumbersome to handle. No analytical solution was derived, and the numerical solutions (c versus f relationship) were not easily obtained as well owing to the complicated, especially twisted nature of the PC function surfaces [37]. Before Ref. [37], PCE solutions in the table form were available [18,36] only for limited values of Poisson's ratio in the limited frequency ranges. Furthermore, the table solutions were provided at unnecessary frequencies for dc because the necessary frequency values can be determined only with information on the bar material (c_o) and bar radius (a) of the user [37]. (Examples of determining the necessary frequencies for dc of the user are available in Ref. [37].) Therefore, unless otherwise specified in existing studies, the table solutions were first interpolated to the solutions for a specific Poisson's ratio (ν) of the researcher's bar material, followed by further interpolation of the formerly interpolated solutions to the solutions at the necessary frequencies for dc for a given bar material (c_o) and bar radius (a). The use of the available solutions is further limited in that some of the solutions in Ref. [36] differ from the solver developed herein, which will be presented subsequently (Sec. 3.3). Only a few studies [29,30,66] independently obtained PCE solutions using in-house (closed source) schemes and presented their solutions for a few Poisson's ratio values in graph forms rather than table values, which limited the application of the solutions.

2.4 Strategy: Bar Property Calibration Together With Verification of the Combined Theories. For the direct verification of the predicted (dispersion-corrected) wave profile with experiment at a given travel distance, two issues must be resolved. First, the bar properties (ν and c_o) should be precisely calibrated in advance. Second, a precise c_{dc} value must be available at the exact frequencies necessary for dc (f_{dc}) for a given bar material (ν and c_o) and bar radius (a).

Regarding the second issue, because of the availability of the open-source solver in a recent study [37], it is now possible to obtain accurate PCE solutions for a wide range of ν values ($0.02 \le \nu \le 0.48$) with down to three decimal places. This solver essentially satisfies most of the dc needs of the (split) Hopkinson bars because the Poisson's ratios of the bar materials are generally reported down to the second decimal place. However, to obtain the c_{dc} versus f_{dc} relationship, c_o and ν information is necessary as mentioned in Introduction, which returns the second issue of obtaining the c_{dc} versus f_{dc} relationship to the first issue of obtaining the calibrated values of the bar properties (c_o and ν). However, precise calibration of both ν and c_o of the bar is never a simple task.

The solution to handling the forgoing fastidious issues is to predict the traveling wave profile for a range of (ν, c_o) sets. That is, to predict the wave profile iteratively by assuming a range of (ν, c_o) sets. If a (ν, c_o) set is determined, which results in a predicted wave profile that reasonably coincides with the experimentally measured wave profile at a given travel distance, the (ν, c_o) set in such a moment in the iteration process is the precisely calibrated bar property. This result of iterative dc; that is, the coincidence of the two profiles, if obtained, is the mutually self-consistent verification of (i) calibrated values of ν and c_o and (ii) combined theories of Fourier and PC, because such coincidence will occur only when the combined theories are correct and, simultaneously, the calibrated values (ν and c_o) are accurate.

Accordingly, an iterative dc is performed herein to investigate the existence of a (ν, c_o) set that can result in a wave profile that reasonably coincides with the traveling wave. For this purpose, an exclusive PCE solver was first developed because the iteration process massively requires accurate PCE solutions for arbitrary ν values down to six decimal places (as will be explained later), whereas the reliable operation of the existing solver in Ref. [37] was verified for ν values down to only three decimal places.

3 Exclusive Pochhammer–Chree Equation Solver for Ground State Excitation

3.1 Necessity of an Exclusive Solver. This section presents an exclusive PCE solver that can be used in the iterative dc process later in this study to calibrate the bar properties (c_o and ν). The two characteristic features of PCE solutions necessary for such a purpose are as follows. First, only the PCE solutions for the first excitation state ($n = 1$) are necessary because the striker impact on the bar usually excites the particle vibration to the first excitation state [18,56,72] (this point will be subsequently verified). Second, although only the PCE solutions for $n = 1$ are necessary, solutions for arbitrary Poisson's ratio values down to six decimal places are needed because most of the general-purpose optimization algorithms, such as "fminseach" in MATLAB®, generally change the value of Poisson's ratio to six decimal places during the iterative optimization process of ν and c_o. Therefore, for a PCE solver to be used in an iterative dc algorithm, it must be able to reliably provide massive PCE solutions for arbitrary Poisson's ratio values to six decimal places.

Considering the mentioned characteristic features of PCE solutions for the iterative dc process, it was decided to develop an exclusive PCE solver for $n = 1$ for the following reasons. First, the existing solver for up to $n = 20$ [37] was verified to function reliably only at 0.001 intervals of Poisson's ratio (only down to three decimal places). Second, if the existing solver is employed in the bar property calibrator program (which will be explained later), a considerable portion of the existing solver for $n \ge 2$ is not used for bar property calibration, whereas the unused portion is intrigued with the overall calibrator program. In a separate trial, the existing solver made the overall bar property calibrator program cumbersome and difficult to modify. Third, thus far, the need for PCE solutions for $n = 1$ for the dc of SHB signals has been very high compared with the solutions for $n \ge 2$, necessitating a more handy but reliable solver for $n = 1$.

In this section, we present an exclusive PCE solver for $n = 1$ that can reliably provide PCE solutions at arbitrary Poisson's ratio values down to six decimal places in an iterative dc process. Compared with the existing solver (up to $n = 20$), the exclusive solver herein should be more robust, straightforward, and ease understanding of the overall bar property calibrator program for any modification. The proposed solver will be verified with reference to the table solutions in existing studies [18,36] for different values of Poisson's ratio. When used in an iterative dc process, its reliability is verified in Sec. 5.

3.2 Solution Scheme. Reference [37] addressed the benefit of the Bancroft version [36] of the PCE in the solution process and expressed it using physics-friendly non-dimensional variables (C and F):

$$G(C, F, \nu) = [C^2(1+\nu) - 1]^2 \Phi\left[2\pi\sqrt{\beta F^2(1+\nu) - (F/C)^2}\right] - [\beta C^2(1+\nu) - 1] \times \left\{C^2(1+\nu) - \Phi\left[2\pi\sqrt{2F^2(1+\nu) - (F/C)^2}\right]\right\} = 0 \quad (4)$$

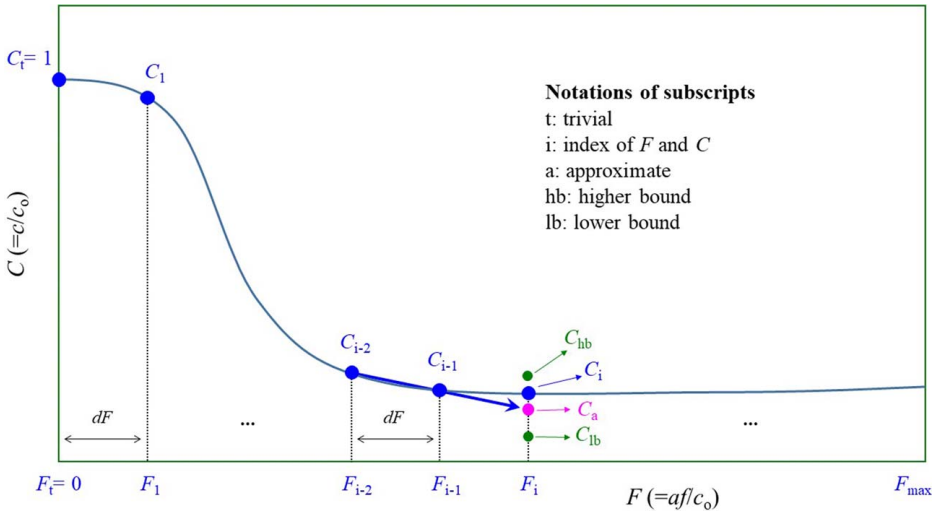

Fig. 1 Scheme to determine the (*F, C*) matrix via linear extrapolation and bisection ($n = 1$)

$$\Phi(y) = yJ_0(y)/J_1(y)$$

$$J_0(y) = \sum_{m=0}^{\infty} \frac{(-1)^m y^{2m}}{2^{2m}(m!)^2}$$

$$J_1(y) = \sum_{m=0}^{\infty} \frac{(-1)^m y^{2m+1}}{2^{2m+1}[(m+1)!]^2}$$

where G is the value of the PC function; J_0 and J_1 are the Bessel functions of the first kind of order zero and one, respectively. The solver herein solves Eq. (4), as in the existing solver [37,38]: the proposed solver determines the C values in a range of F values for a given ν value when $G = 0$.

As illustrated in Ref. [37], the PCE has an infinite number of function surfaces with versatile slopes, which leads to an infinite number of C–F solution curves (dispersion curves) that make the G value zero. The schematic of the dispersion curve for the first excitation mode ($n = 1$) is illustrated in Fig. 1. Similar to the existing solver [37], this study is based on an iterative root-finding process. However, in the current solver, the search algorithm for C solutions starts from the F value of zero in the C–F domain, as illustrated in Fig. 1, whereas the existing solver [37] sought solutions from the intermediate F value ($6 \le F \le 11$ depending on the Poisson's ratio). The consequences of the mentioned differences are discussed later (Sec. 3.4).

The scheme of the current solver is shown in Fig. 1. The proposed solver utilizes the trivial solution of $C_t = 1$ at $F_t = 0$ as the first initial solution. The second initial solution (C_1) is determined at F_1 ($= 1 \times dF = 0.001$). Then, the PC function value (G) is monitored at F_1 for a range of C values from 1 to 0.99 at C intervals of $dC = 1 \times 10^{-6}$. Once the sign of the PC function value (G) changes, the C values before and after the sign change are taken as C_{hb} and C_{lb}, respectively. C_1 is subsequently determined using the bisection method. Note that the trivial solution ($C_t = 1$ at $F_t = 0$) is unnecessary in dc.

Once two initial solutions (C_t and C_1 at F_t and F_1, respectively) are available, the current solver utilizes two previous solutions C_{i-2} and C_{i-1} at F_{i-2} and F_{i-1}, respectively, to predict the approximate solution (C_a) at current F_i via linear extrapolation (subscript i is the index of F and C; subscript a denotes "approximate"). It finally determines C_i at the independent variable F_i via the bisection method using two bound values (C_{hb} and C_{lb}), which process is described in Ref. [37]. The determined C value (C_i) is accurate down to the ninth decimal place, as the tolerance limit in the bisection method is set herein as 1×10^{-10}.

In general, the determined (F, C) matrix differs from the (F_{dc}, C_{dc}) matrix which is used for dc (see Ref. [37]). The (F, C) matrix is typically obtained at finer F intervals ($dF = 0.001$) than the necessary interval (dF_{dc}) of the (F_{dc}, C_{dc}) matrix. If necessary, the user can adjust the dF value of the proposed solver (the dF_{dc} value is determined based on the need for dc).

Once the (F, C) matrix is obtained (Fig. 1), the proposed solver determines the (F_{dc}, C_{dc}) matrix by linearly *interpolating* the (F, C) matrix at each F_{dc} component. The schematic of the linear interpolation process is illustrated in Fig. 2. In Fig. 2, subscript k is the index of F_{dc} and C_{dc}. The proposed solver first obtains the approximate solution C_a at the current $F_{dc,k}$ via the linear interpolation of the C solutions at F_{i-1} and F_i, between where the current $F_{dc,k}$ is located. Subsequently, $C_{dc,k}$ values at $F_{dc,k}$ are searched at intervals of $dC_{dc} = 1 \times 10^{-6}$ until C_{dc_hb} and C_{dc_lb} are found, where the PC function (G) values have different signs. Next, the $C_{dc,k}$ solution at the current $F_{dc,k}$ is obtained via the bisection method using C_{dc_hb} and C_{dc_lb} values as the two bounds for the solution.

The above algorithms (illustrated in Figs. 1 and 2) consist of the main part of the solver and two subroutines, as illustrated in Fig. 3. Briefing their roles, the main part performs the overall procedures mentioned above (summarized in Fig. 3), and calls the subroutines when in need of the PC function value (subroutine "pcf") or the C (or C_{dc}) value determined using the bisection method (subroutine "bisectc"). The main part provides ν, C (or C_{dc}), and F (or F_{dc}) values to the subroutine "pcf", and ν and two bound values of C (or C_{dc}) at a given F (or F_{dc}) to the subroutine "bisectc". The aforementioned algorithms were implemented in MATLAB® software (PCE_solver_n1.m), which is available online [41]. The current solver writes the finally obtained (F_{dc}, C_{dc}) matrix to "Cdc-Fdc.xlsx" file.

3.3 Solver Verification. The reliability of the proposed solver is verified by comparing the obtained solutions (accurate to the ninth decimal place) with those studied by Bancroft [36] (available to the fifth decimal place) for a range of Poisson's ratios. Figure 4 compares the current solutions with those in Bancroft [36]. To avoid spatial crowding, Fig. 4 is divided into two parts depending on the values of Poisson's ratio: Fig. 4(*a*) for $\nu = 0.1$, 0.2, 0.3, and 0.4, and Fig. 4(*b*) for $\nu = 0.15$, 0.25, and 0.35. The C values in Ref. [36] were listed in table at L ($= a/\Lambda$) intervals of 0.025 or 0.1, which were transformed herein into C–F domain solutions; the results are presented in Fig. 4 as open circles. In this figure, the intervals in Bancroft's data are irregular in the *F-axis* owing to the transformation from L to F ($F = CL$). Figure 4 shows the current solutions obtained at constant F intervals of 0.01 (marked as "×"). C solutions at regular F intervals are necessary for dc.

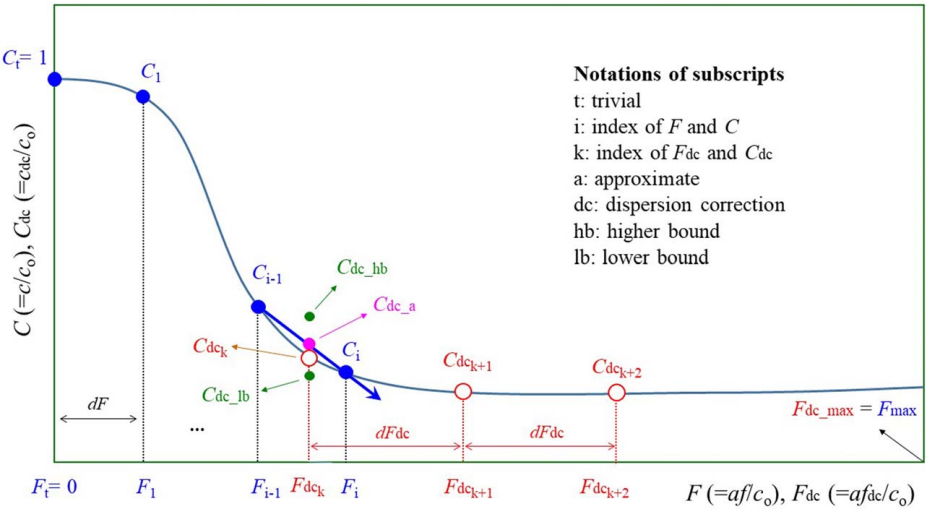

Fig. 2 Scheme to determine the (F_{dc}, C_{dc}) matrix from the (F, C) matrix via linear interpolation and bisection ($n = 1$)

In Fig. 4(*a*), the current solutions are consistent with those in Bancroft [36] for $\nu = 0.1$, 0.2, 0.3, and 0.4, which verifies the current solver. In Fig. 4(*b*), the consistency of the current solutions with those in Bancroft [36] is observed for $\nu = 0.25$ and 0.35, which also verifies the current solver. However, a notable discrepancy is observed for $\nu = 0.15$. In separate trials, the solver in Ref. [36] resulted in the same C values as the current solver, down to nine decimal places of C for all values of Poisson's ratio considered in Fig. 4. The C solutions for $\nu = 0.15$ in Bancroft [36], especially in the range of approximately $0.25 \le F \le 0.4$ need to be further verified by other solvers.

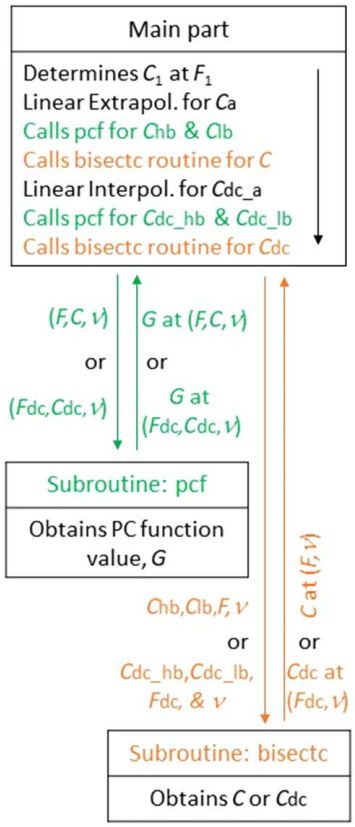

Fig. 3 Feedbacks among the main part, subroutine "pcf," and subroutine "bisectc" in the current PCE solver (PCE_solver_n1.m)

3.4 Benefit of the Exclusive Solver. The C vs. F solution curves for $n \ge 2$ are unavailable in the low F regime (below the cut-off F values) [37]. Under such circumstances, the existing solver [37] obtained the C–F solutions using the initial two solutions at two intermediate F values that belong to the range of $6 \le F \le 11$ because all the solution curves up to the 20th order are available and can be suitably determined in this F range. If the C solution is searched (with finite C intervals) at an overly higher F value than the ones in this F range, the C solution is evanescent, which gnaws the robustness of the PCE solver. For the first excitation state ($n = 1$), the dispersion curve is available down to $F = 0$ (no cut-off F value). Therefore, the exclusive PCE solver herein employs the trivial solution ($C_t = 1$ at $F_t = 0$) as an initial solution and determines another initial solution in the vicinity of the trivial solution.

The characteristic features of the current algorithm are as follows. The necessity of determining only one initial solution in the vicinity of the trivial solution accelerates the overall solver as compared with the existing solver [37]. Second, because the slope of the PC function surface varies slightly in the vicinity of the trivial solution ($F = 0$), higher reliability is imparted in determining the initial solution than in the case where the initial solutions are determined at increased F values [37]. Finally, the succinct nature of the current solver avoids any unfavorable routine in the complicated solver for $n \le 20$ in Ref. [37].

The aforementioned characteristics of the current solver, and the flexibility in setting the dF value (as in the existing solver [37]), would contribute to the robustness of the proposed exclusive solver for $n = 1$. The reliability of the current solver when used in a general-purpose optimization algorithm, that requests massive C–F solutions for various ν values down to six decimal places, is verified later (Sec. 5).

Once the bar properties are calibrated using our calibrator program (dispersion_correction_iteration.m [41]), the calibrated value of Poisson's ratio of the bar can be truncated to three decimal places. Then, the existing solver in Ref. [37] can be used to obtain PC solutions up to $n = 20$, which are specific for the calibrated property of the researcher's bar. A higher-order dc using the solver in Ref. [37] for up to $n = 20$ is worthwhile only when the (S)HB properties are well calibrated using the solver herein for $n = 1$. Therefore, the usage of the solver presented in Ref. [37] for up to $n = 20$ is supplemented by the current solver for $n = 1$ [41].

4 Bar Property Calibration

4.1 Experiment. The specification of the bar material requested to a local supplier was Maraging steel C350. When the

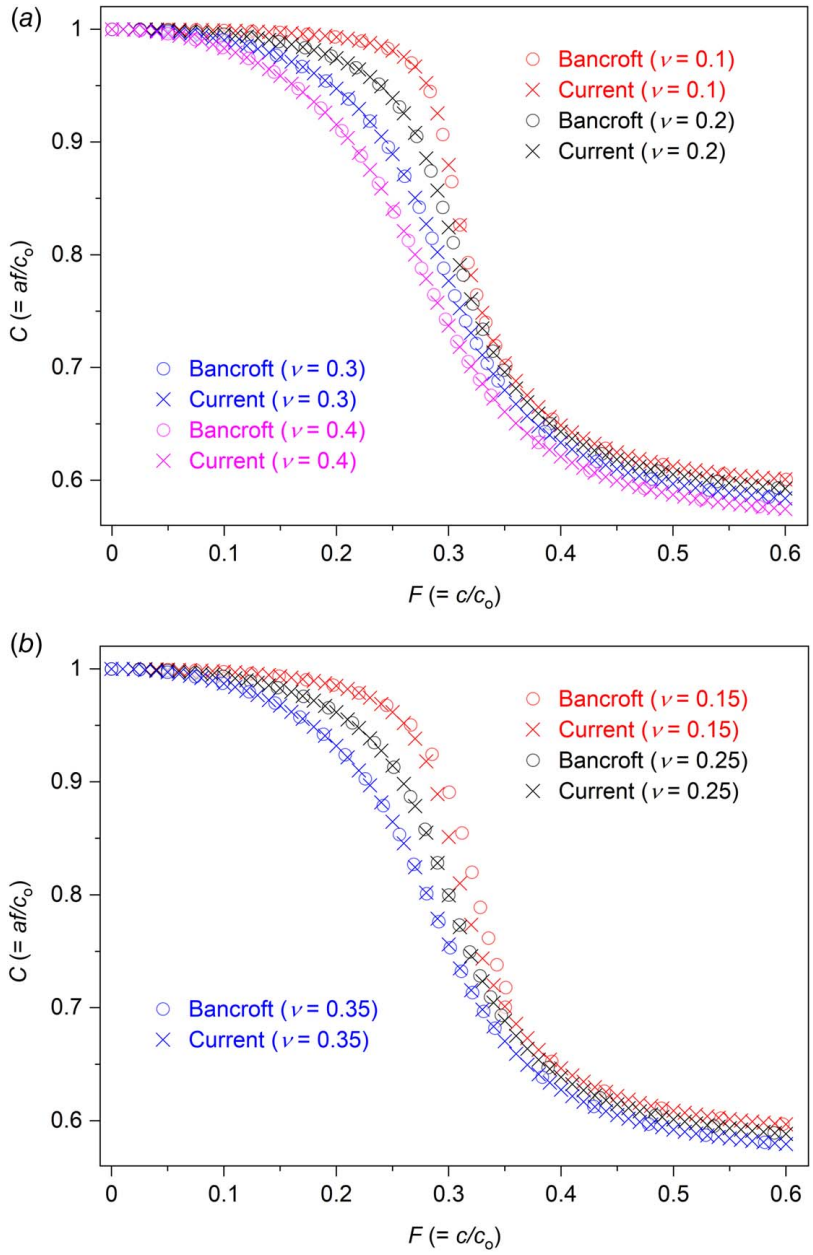

Fig. 4 Comparison of the current solutions for $n = 1$ with those in Bancroft [36]: (*a*) $\nu = 0.1$, 0.2, 0.3, and 0.4; (*b*) $\nu = 0.15$, 0.25, and 0.35

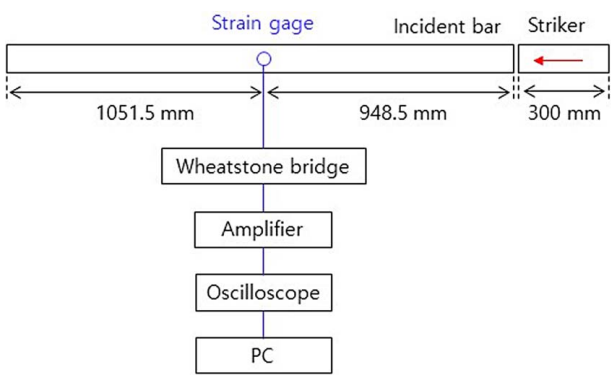

Fig. 5 Schematic of the experimental setup

bar was supplied to the author's laboratory, one end surface of the bar (19.1 mm in diameter) was indented to mark "C350". The bar was cut to dimensions of 2000 and 300 mm for the bar and striker, respectively.

A schematic of the experimental setup is shown in Fig. 5. The striker collided with the bar at a speed of 11.7 m/s, as measured using a high-speed camera. There was neither a specimen nor a transmission bar (bar-alone or bar-apart test). The profile of the elastic wave generated in the bar was measured using a strain gauge attached to the surface of the bar at 948.5 mm from the impact surface (1,051.5 mm from the rear end). The size of the strain gage (metallic part) was 1.1×1.3 mm (120 ohms; gage factor 2.1). This strain gauge formed a 1/4 bridge of the Wheatstone bridge circuit. The output signal of the Wheatstone bridge was amplified and transferred to an oscilloscope that digitized the incoming analog signal at a sampling

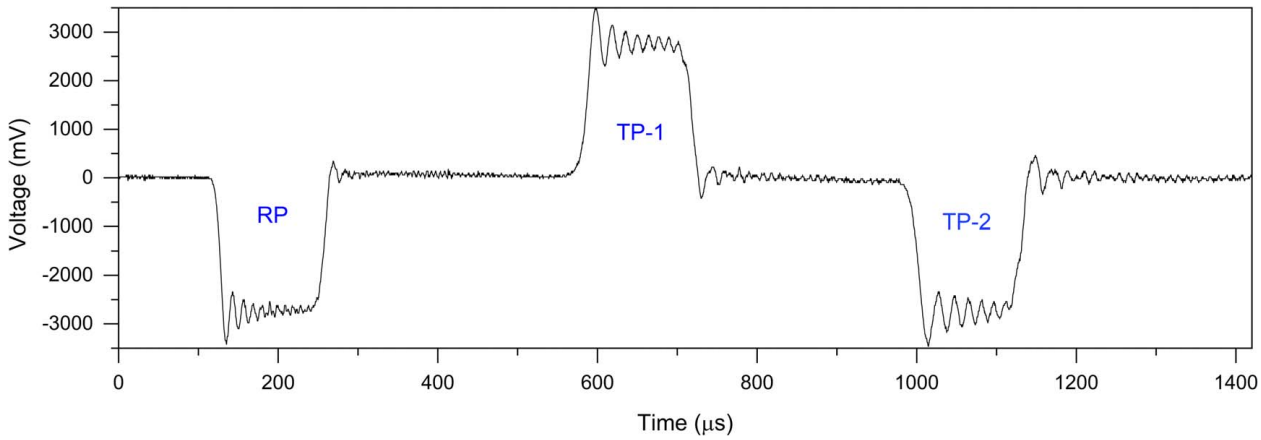

Fig. 6 Measured strain signal at the position of the strain gauge. RP denotes the reference pulse, TP-1 denotes the first traveled pulse coming from the left-end surface of the bar, and TP-2 denotes the second traveled pulse coming from the right-end surface of the bar.

rate of 5 MHz. The digitized data were stored on a personal computer.

4.2 Recorded Wave Profile. The measured strain signal on the bar surface is shown in Fig. 6, where the positive sign denotes tension. In Fig. 6, the vertical position of the entire profile was shifted slightly arbitrarily after the measurement for the baseline alignment. The time origin was set arbitrarily. The data for Fig. 6 are available in Ref. [41] (experiment.csv and dispersion_correction.xlsm).

In Fig. 6, the pulse marked RP is the incident strain pulse from the impact surface. This pulse was used as the reference pulse (RP), which will be used later for mathematical modeling (Fourier synthesis), followed by a phase shift. The compressive incident pulse (RP) reflects at the rear end of the bar and forms a tensile wave from the end surface owing to impedance mismatch at the rear surface [13]. The first traveled pulse, denoted as TP-1,

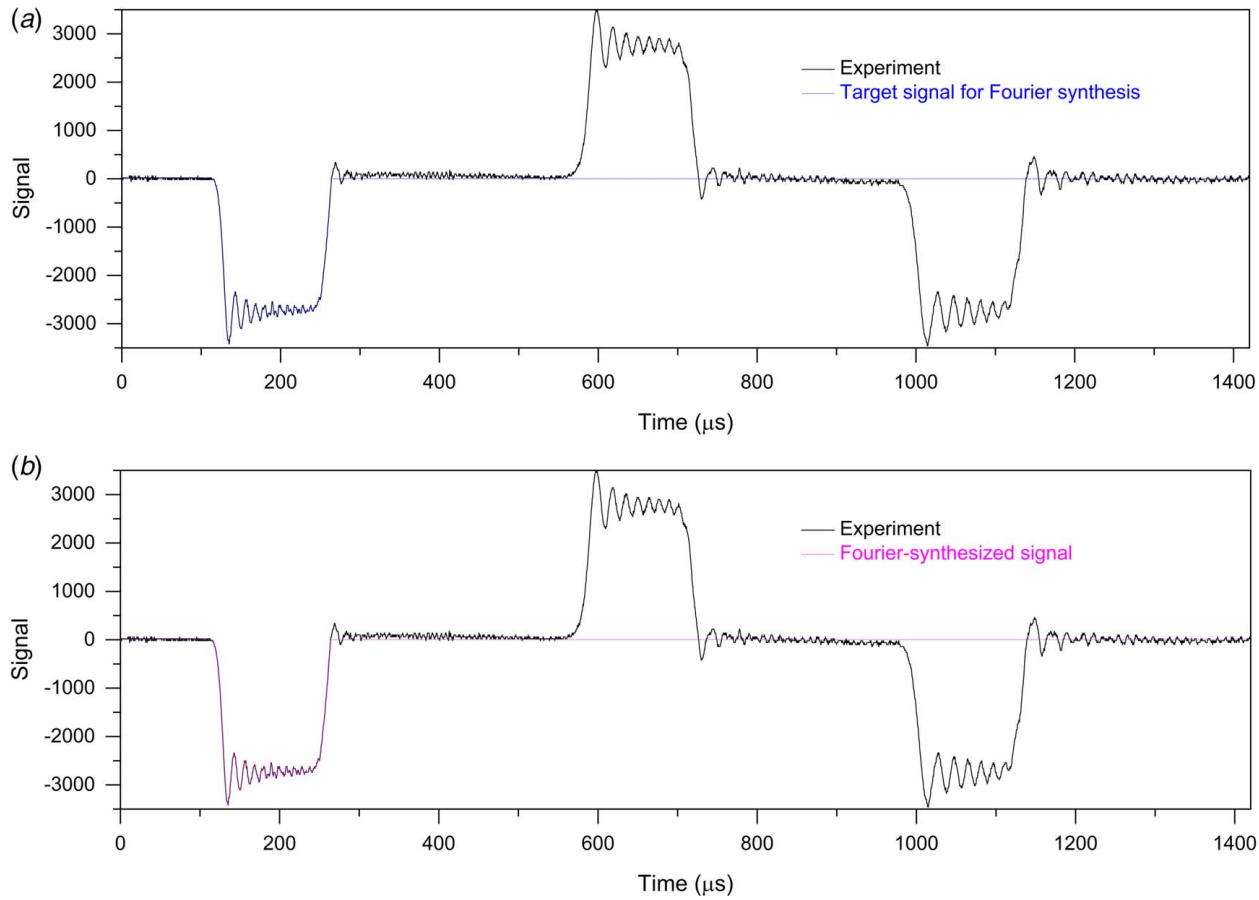

Fig. 7 (*a*) Target signal for Fourier synthesis and (*b*) the Fourier-synthesized signal using Eqs. (5)–(8). The ordinate is the shape function $x(t)$ in Eq. (5).

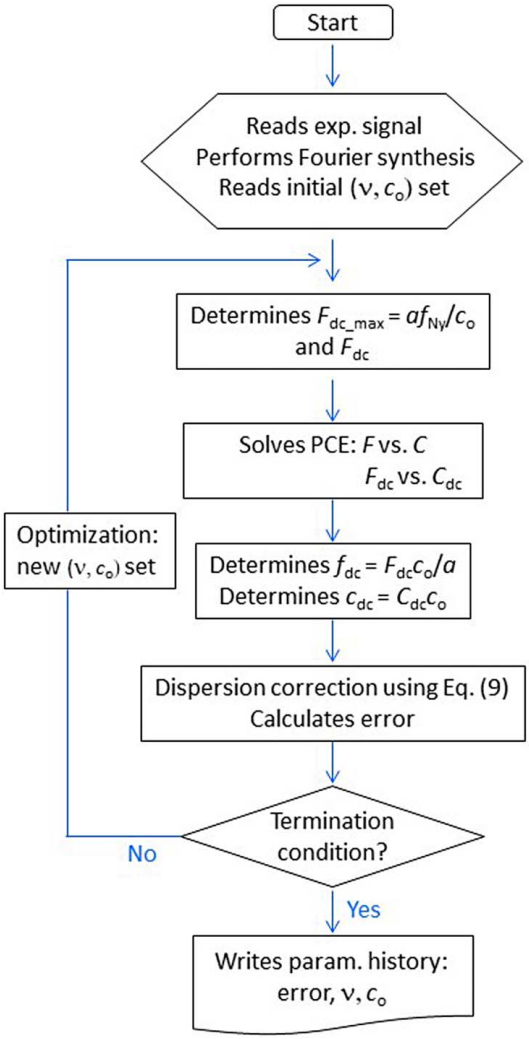

Fig. 8 Flowchart for the iterative dc algorithm in the calibrator program (dispersion_correction_iteration.m)

arrived from the left-end surface of the bar. The travel distance from RP to TP-1 was 2103 mm (z_1). TP-2 arrived from the right-end surface (i.e., the former impact surface) of the bar. The travel distance from RP to TP-2 was 4000 mm (z_2).

4.3 Target Signal Preparation. Fourier synthesis is the process of mathematically modeling a periodic signal by combining sine and/or cosine waves in certain proportions whose frequencies are multiples of the lowest, or fundamental, frequency. The signal to be used for Fourier synthesis is called herein the target signal for Fourier synthesis. For the convenience of explanation, the prepared target signal is illustrated in advance in Fig. 7(*a*) before explaining how it was prepared.

For target signal preparation, the onset point of the RP was determined based on visual inspection. As observed in Fig. 7(*a*), the ordinate values before and at the onset point of the incident pulse (RP) were zero-padded in the target signal.

The endpoint of the RP was selected as the point when the pulse magnitude in the releasing part of the wave changed sign for the first time. The ordinate value after and at the endpoint of the RP were also zero-padded in the target signal. The reason the endpoint of the RP was selected as such is as follows. The tail part of the RP is composed of sluggish wave components with higher frequencies; the sluggish nature explains why they are located at the tail part. Therefore, the wave components in the tail part are increasingly behind the main pulse as the RP travels in the bar. From tests using the Excel® template (dispersion_correction.xlsm), the inclusion of the tail part of the RP into the target signal does not influence the main part of the dispersion-corrected wave profile at a given travel distance; however, it only complicates the far-tail part of the dispersion-corrected wave profile.

The recorded data located between the start and end times of the RP pulse were included in the target signal data. The determination of the start and endpoints of the RP can be assisted using the Excel® template (dispersion_correction.xlsm) in Ref. [41].

4.4 Fourier Synthesis. The time-dependent pulse in Fig. 7(*a*) (target signal) can be described using the framework $X(t) = Mx(t)$, where X is the measured quantity (usually with a dimension; mV herein), M is the magnitude constant with a dimension of X, $x(t)$ is a non-dimensional shape function, and t is the time. M is set to 1 mV, and thus, the ordinate of Fig. 7 is $x(t)$. The elastic pulse recorded at discrete time points can be mathematically modeled (synthesized) using a Fourier series:

$$x(n\Delta t) = \frac{A_0}{2} \sum_{k=0}^{K} [A_k \cos(2\pi k f_0 n\Delta t) + B_k \sin(2\pi k f_0 n\Delta t)] \quad (5)$$

where n is the index to describe time points spanning from 0 to $N_t - 1$; N_t is the number of data points in the time window with a fundamental period ($t_0 = N_t\Delta t$); Δt is the time interval for sampling; f_0 is the fundamental frequency ($=1/t_0$); k is the index to describe the terms of the Fourier series spanning from 1 to K; K is the summation limit of the Fourier series, which is the Nyquist number (N_y); A_0, A_k, and B_k are the Fourier coefficients given as:

$$A_0 = \frac{2}{T_0} \int_0^{t_0} x(t)dt \quad (6)$$

$$A_k = \frac{2}{T_0} \int_0^{t_0} x(t) \cos(2\pi k f_0 t)dt \quad (7)$$

$$B_k = \frac{2}{T_0} \int_0^{t_0} x(t) \sin(2\pi k f_0 t)dt \quad (8)$$

The target profile shown in Fig. 7(*a*) was synthesized using Eqs. (5)–(8). The conditions for Fourier synthesis were as follows: $t_0 = 1420$ μs, $f_0 = 1/t_0 = 704.225325$ Hz, $df = f_0$, $\Delta t = 0.2$ μs, $N_t = t_0/\Delta t = 7100$, $f_s = 1/\Delta t = 5$ MHz, $f_{Ny} = f_s/2 = 2.5$ MHz, $K = N_y = f_{Ny}/df = 3550$. The Fourier synthesis of the target signal using Eqs. (5)–(8) can be assisted using an Excel® template (dispersion_correction.xlsx) [41]. The signal synthesized using the Excel® template is shown in Fig. 7(*b*). As shown in Fig. 7(*b*), the synthesized signal successfully describes the target signal that includes the main part of the experimentally measured RP.

4.5 Dispersion Correction (Phase Shift). As the elastic stress wave travels through the bar, the kth frequency component (kf_0) with a speed of c_k travels a distance Δz in time $\Delta z/c_k$, which is the time lag of the wave component with the kth frequency (kf_0). Hence, the Fourier series expression for the stress pulse after traveling a distance Δz is:

$$X(n\Delta t) = \frac{A_0}{2} \sum_{k=0}^{K} \left\{ A_k \cos\left[2\pi k f_0 \left(n\Delta t - \frac{\Delta z}{c_k} \right) \right] + B_k \sin\left[2\pi k f_0 \left(n\Delta t - \frac{\Delta z}{c_k} \right) \right] \right\} \quad (9)$$

where Δz is positive for forward travel and negative for backward travel. Equation (9) describes the translation of each wave component with a particular frequency by an amount of $+\Delta z/c_k$ in the time axis. Note that F_{dc} and C_{dc} in numerically solving the PCE was derived from the concept of f_{dc} and c_{dc}, respectively, which are exactly required f and c values, respectively, in dc. Correlating the f_{dc} and c_{dc} with the variables in Eq. (9), $f_{dc,k} = kf_0$ and $c_{dc,k} = c_k$ (k = 1,2,3…).

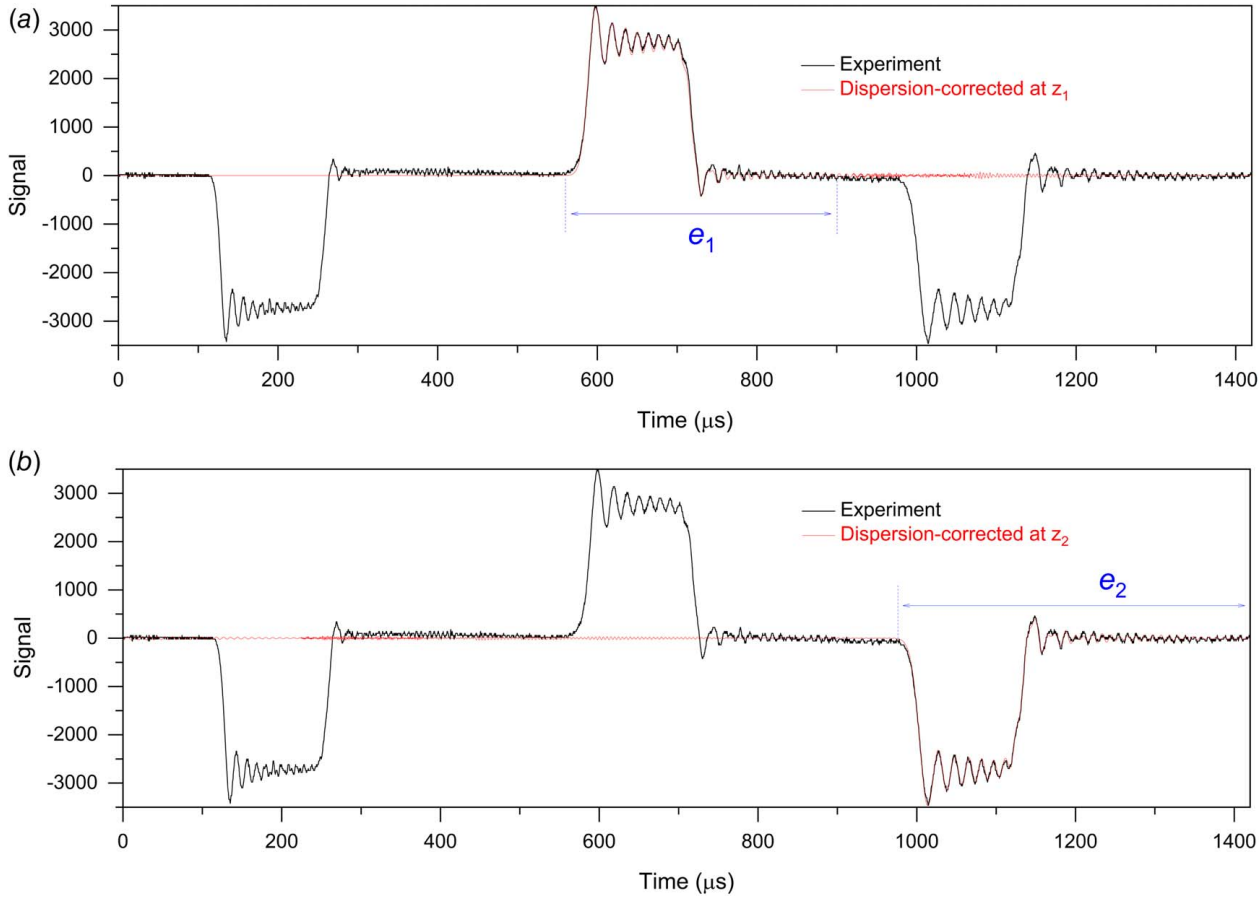

Fig. 9 The predicted (dispersion corrected, i.e., phase-shifted) profiles when the ν and c_o set is optimized ($\nu = 0.335050$, $c_o = 4588.233496$ m/s) using the iterative dc program (dispersion_correction_iteration.m) at travel distances of (*a*) $z_1 = 2103$ mm and (*b*) $z_2 = 4000$ mm

4.6 Iterative Dispersion Correction. The dc process described in the previous sections can be suitably performed using the Excel® template (dispersion_correction.xlsm) and the PCE solver (PCE_solver_n1.m) available in Ref. [41], provided the bar sound speed (c_o) and Poisson's ratio (ν) were calibrated in advance. For mutually self-consistent verification of the combined theories, and the calibrated set of (ν, c_o), iterative dc is necessary. Thus, a calibrator program (dispersion_correction_iteration.m) was prepared, which included the exclusive PCE solver developed herein (PCE_solver_n1.m). The algorithm of the calibrator program is illustrated in Fig. 8.

As shown in Fig. 8, once Fourier synthesis is performed, the iterative dc starts with the initial guess values of ν and c_o. The program then performs the first run of dc, followed by error calculation of the dispersion-corrected (predicted) profiles with reference to the measured profiles at z_1 and z_2. From the second run of the foregoing processes, the ν and c_o set is determined using the general-purpose optimization function "fminsearch" available in MATLAB.® "fminsearch" is an unconstrained nonlinear optimization function that determines the minimum scalar function of several variables, starting from an initial estimate [73]. The iteration of dc continues until the discrepancy (error) between the predicted wave profiles and the experimentally measured profiles is diminished below a preset condition [40].

The error between the predicted and experimentally measured pulse profiles at travel distances z_1 or z_2 was quantified as follows:

$$\text{Error } (\%) = \frac{\sum_{i=1}^{i=N_p} |x_i^{dc} - x_i^{exp}|}{N_p x_{max}^{exp}} \times 100 \tag{10}$$

where i is the index of the time data of the pulse at the travel distance of either z_1 or z_2; x is the magnitude of the nondimensional shape function, $x(t)$; superscripts dc and exp denote dispersion corrected and experiment, respectively; N_p is the number of data in a given pulse (TP-1 or TP-2); and x_{max}^{exp} is the maximum magnitude (positive) of the measured pulse in TP-1 or TP-2. $\sum_{i=1}^{i=N_p} |x_i^{dc} - x_i^{exp}|/N_p$ is the average absolute deviation. (These notations are explained here as Eq. (10) is limited to the error calculation instead of dc.). Equation (10) describes the concept of average absolute deviation with reference to the maximum pulse height of the experimental pulse.

To calculate the error of a dispersion-corrected pulse with reference to the traveled pulse in the experiment, the error calculation range must be defined. It started from the onset point of each traveled pulse, as shown in Fig. 9. The tail part that follows the main pulse is suggested to be included in the error calculation range because of the reason that will be explained later. Consequently, the endpoint of the error calculation range was selected arbitrarily to include the tail part. The selected error calculation ranges for the two traveled pulses are illustrated in Fig. 9 as e_1 and e_2. Unless terminated by the count limit for the iteration loop [40], the calibrator program exits the iteration loop when both ν and c_o values with six decimal places do not vary significantly as the iterations continue.

5 Discussion

5.1 Bar Property Calibration. The calibrator program herein [41] successfully found the (ν, c_o) set, at which condition the dc of the reference pulse created wave profiles that reasonably coincided with the experimentally measured profiles at travel distances of z_1 and z_2. Figure 9 compares the predicted (dispersion-corrected) profiles with the experimentally measured profiles when $\nu = 0.335050$

and $c_o = 4588.233496$ m/s. As mentioned, e_1 (560.6–900.0 μs) and e_2 (977.8–1419.8 μs) in Fig. 9 denote the error calculation ranges for the traveled pulses at z_1 and z_2, respectively, which were set arbitrarily to monitor the error in predicting the respective pulse and its tail part.

In Fig. 9, the error values of the dispersion-corrected pulses with reference to the experimental signal were 1.479843 and 1.105220% (average error was 1.292531%) at travel distances of $z_1 = 2103$ and $z_2 = 4000$ mm, respectively. The origins of such errors may include (i) the change in diameter of the bar and striker along the axial direction, (ii) imperfect planes of impact and wave reflection; that is, imperfect end surfaces of the bar and striker, and (iii) imperfect alignment of the striker and bar. Despite such error sources in the experiment, the coincidence of the predicted (dispersion-corrected) wave profiles to the measured profiles is remarkable, which indicates the reliability of the calibrated values of c_o and ν of the bar used in this study. In separate trials [40], the calibrated values were insensitive to the initial guess values. Based on a number of trials with different initial guess values for the calibrator program, Ref. [40] calibrated the values of c_o and ν to 0.335050 and 4588.2335 m/s, respectively, for the experimental profile considered.

5.2 Verification of the Combined Theories. The remarkable consistency of the experimental and the predicted profiles in Fig. 9 is semanticizable in a number of points, as follows. First, the observed consistency is a direct experimental verification of the Fourier theory (using a physical quantity; that is, mechanical vibration), which states that any *periodic* event can be described using the sum of sine and/or cosine waves with multiples of the fundamental frequency (i.e., waves with varying sound speeds, i.e., wavelengths). The use of Eqs. (1)–(5) means this study mathematically treats the one-time event presented in Fig. 2 as a periodic event with a period of $t_0 =$ 1420 μs (fundamental frequency, $f_0 = 704.225325$ Hz).

Second, the result in Fig. 9 also experimentally verifies the PC theory [18,32–41] and its solver [37,41] because, as in the case of the Fourier theory, the consistency of the dispersion-corrected profiles with the measured profiles is never achieved unless the C_{dc} versus F_{dc} relationship obtained by solving the PCE is correct. Further, the result in Fig. 9 verifies that the first excitation mode in the PC theory reasonably describes the propagation of an elastic wave generated via striker impact on the bar [18,56,72].

As mentioned earlier, the result of iterative dc, that is, the coincidence of the two profiles in Fig. 9, mutually self-consistently verifies (i) the combined theories of Fourier and PC that resulted in the consistency and (ii) calibrated values of ν and c_o. Such successful verification is attributed to the availability of the (i) calibrator program with iterative dc algorithm and (ii) exclusive PCE solver (which massively and reliably provided the PCE solutions for Poisson's ratios down to six decimal places upon request of the iterative dc algorithm).

The verification of the combined theories of Fourier and PC imparts physical meaning to each hill and valley in the plateau region of the elastic pulse after traveling some distances (Fig. 9). The hills and valleys in the plateau region are the physical corollaries resulting from the travel of a series of wave components with different sound speeds (frequencies), as predicted by the combined theories of Fourier and PC. The hills and valleys, even in the tail part of the traveling pulse, are similar to those in the plateau region of the main pulse; the tail parts of the traveled pulses are not merely meaningless noise-associated fluctuations but result from sluggish high-frequency wave components that formerly belonged to the plateau region (primary pulse) at a shorter travel distance. Because of such significance of the tail part, the ranges of the error calculation (e_1 and e_2 in Fig. 9) were selected to be wider than the main traveled pulses (TP-1 and TP-2, respectively). It means that the wave components with higher frequencies leak from the plateau part of a traveling pulse to form the tail. However, the influence of the leakage on the overall pulse magnitude is negligible (see Fig. 9) in an SHB test, where the travel distance before measuring the pulse signal is less than approximately three meters.

5.3 Contribution to the Bar Technology. Once the sound speed (c_o) and Poisson's ratio (ν) of the user's bar are calibrated using the proposed method and templates [41], the higher-mode vibration signals generated via the impact of explosive and/or blast waves on HB may be measured at two travel distances. Then, the blast wave profile at one of the travel distances can be predicted from another via dc using the PCE solver in Refs. [37,38]. This solver can provide PCE solutions up to an order of $n = 20$. The consistency of the predicted profiles with the experimentally measured wave profile with higher-mode vibrations, if observed, will further verify the combined theories of Fourier and PC, which should subsequently ensure the reliability of the predicted blast wave profiles at the front surface of the HB.

Thus far, no international standard has been established for the SHB test despite its extensive exploitation in measuring the stress–strain curves of versatile materials at high strain rates [11]. Once c_o is calibrated, the density (ρ) of a piece of bar material can be measured using a method based on the Archimedes principle [74,75] or using a pycnometer [76]. The elastic modulus (E_o) of the bar can then be determined using c_o and ρ information: $E_o = \rho c_o^2$ (ρ is the bar density). Because the stress, strain rate, and strain values of the specimens determined via the SHB test directly depend on c_o and E_o values [1–16], the precise calibration of the bar sound speed (c_o) using the method and templates herein [41] will contribute to the reliable measurement of stress–strain and strain rate–strain curves using an SHB. The strain rate equation available in Ref. [12] enables researchers to verify the reliability of an SHB experiment via the correlation of the stress–strain curve with the strain rate–strain curve. Therefore, the calibration of the speed of sound of the bar (c_o) and the strain rate equation [12] may contribute to the standardization of the SHB test. The reliability of the direct impact bar test [77–80] also resorts to the precisely calibrated bar properties (ν, ρ, c_o, and E_o). The c_o calibration of the bar also renders the 1D equations [13] on the bar technology more useful.

The calibrated values of ν, ρ, and E_o enable an explicit finite element analysis of the events achieved in the (S)HB and the direct impact bar. The foregoing quantities can then be used for inverse engineering [81] of many bar technology events. For instance, the constitutive parameters of a specimen or small structure can be identified via simulations of (i) the plastic deformation of small structures (or specimens) sandwiched between two elastic bars and (ii) resultant SHB wave signals. The material properties of the specimen (e.g., constitutive parameters) inputted to the simulation can be varied until the simulated and measured bar wave profiles in the bar overlap, which eventually allows the determination of the specimen properties. Precise calibration of the bar properties is a prerequisite for such simulation-based inverse engineering of many events in bar technology.

5.4 Further Discussion. In this study, the surface strain waves at two travel distances were measured (Fig. 2), and the corresponding surface wave profiles were predicted (Fig. 6); this is called the standard dc process. Magnitude correction [27,28,63] refers to the process of obtaining the (i) average strain over the bar cross section from the surface strain and (ii) the dynamic elastic modulus that converts the bar strain to bar stress. This study is limited to standard dc because the calibration of the bar properties requires only the phase shift (Eq. (5)) of the wave profiles measured on the bar surface.

Standard dc can be performed either in the time [18,60] or frequency domain [26–30,55–59,61–66]. If performed correctly, both approaches will result in the same dispersion-corrected pulse profiles. Therefore, there is no reason that one type of approach should be used predominantly over another (their usage depends on the choice of the user); however, the time-domain approach employed is simple, straightforward, and easy to understand. Dispersion correction via the two approaches will be compared in a review paper elsewhere.

6 Conclusion

The process of calibrating the 1D sound speed (zero-frequency sound speed, c_o) and Poisson's ratio (ν) of an (S)HB is presented. The process comprises Fourier synthesis and iterative dc (time-domain phase shift) of the elastic pulse generated via striker impact on a circular bar.

An exclusive PCE solver for ground state excitation was developed, as it was necessary for dc herein. The reliability of the developed solver was verified by comparison with table solutions in previous studies. The developed solver could reliably provide PCE solutions according to the massive request of the iteration algorithm for Poisson's ratios with six decimal places.

At each iteration in the iterative dc process, a set of c_o and ν was assumed, and the sound speed versus frequency (c_{dc} versus f_{dc}) relationship under the assumed set was obtained using the PCE solver developed herein. Subsequently, each constituting wave of the overall elastic pulse was phase shifted (dispersion-corrected) using the c_{dc}–f_{dc} relationship. The c_o and ν values of the bar were determined in the iteration process when the predicted (phase-shifted, dispersion-corrected) overall pulse profiles were reasonably consistent with the measured profiles at two travel distances (2103 and 4000 mm) in the bar.

The observed consistency of the predicted wave profiles with the measured profiles at the calibrated (ν, c_o) set was the mutually self-consistent verification of (i) the calibrated values of ν and c_o and (ii) combined theories of Fourier and PC that resulted in the coincidence of the wave profiles. As revealed by this verification, the hills and valleys in the plateau part as well as the tail part of a traveling wave are the physical corollaries resulting from the travel of a series of wave components with different sound speeds (frequencies), as predicted by the combined theories. The calibrated values of ν and c_o may contribute to the contemporary bar technology in (i) further verifying the combined theories when higher-mode vibrations are present; (ii) increasing the reliability of the stress–strain and strain rate–strain curves measured using SHB; (iii) utilizing the strain rate equation for the verification of an SHB experiment; (iv) utilizing 1D equations; and (v) inverse engineering of SHB events.

Acknowledgment

The author appreciates Jae Eon Kim and Jun Moo Lee for their technical assistance.

Funding Data

- This study was financially supported by a National Research Foundation of Korea Grant under Contract No. 2020R1A2C2009083 funded by the Ministry of Science and Technology (Korea).

Conflict of Interest

There are no conflicts of interest.

Data Availability Statement

Data are openly available in a public repository [41]. The datasets generated and supporting the findings of this article are also obtainable from the corresponding author upon reasonable request.

Nomenclature for Dispersion Correction

a = bar radius (m)
c = sound speed of a wave with frequency f (m/s)
f = frequency (Hz)
t = time (s)
C = normalized sound speed ($=c/c_o$)
F = normalized frequency ($=af/c_o$)
K = summation limit in Fourier synthesis ($=N_{dc}=N_y$)
L = normalized wavelength ($=a/\Lambda$)
c_{dc} = c value used in dispersion correction (m/s)
c_o = one-dimensional sound speed (m/s). c at $f=0$ (or $a=0$)
dF_{dc} = F interval in dispersion correction
df_{dc} = f interval in dispersion correction
df = f interval
dF = F interval
Δt = sampling time interval (s)
Δz = travel distance (m)
f_{dc} = f value used in dispersion correction (Hz)
f_0 = fundamental frequency ($=1/t_0$; Hz)
f_{Ny} = Nyquist frequency ($=f_s/2$; Hz)
f_s = sampling frequency ($=1/\Delta t$; Hz)
t_0 = fundamental period (s)
C_{dc} = C value used in dispersion correction
F_{max} = maximum F value
F_{dc} = F value used in dispersion correction
F_{dc_max} = maximum F value in dispersion correction
Λ = wavelength (m)
N_{dc} = number of F (f) components in dispersion correction ($=N_y$)
N_p = number of data in a traveled pulse in the experiment
N_t = number of data in the time window ($=t_0/\Delta t$)
N_y = Nyquist number ($=f_{Ny}/\Delta f=N_{dc}$)
ν = Poisson's ratio

References

[1] Kolsky, H., 1949, "An Investigation of the Mechanical Properties of Materials at Very High Rates of Loading," Proc. Phys. Soc. Sect. B, **62**(11), pp. 676–700.
[2] Davies, E. D. H., and Hunter, S. C., 1963, "The Dynamic Compression Testing of Solids by the Method of the Split Hopkinson Pressure Bar," J. Mech. Phys. Solids, **11**(3), pp. 155–179.
[3] Jahsman, W. E., 1971, "Reexamination of the Kolsky Technique for Measuring Dynamic Material Behavior," ASME J. Appl. Mech., **38**(1), pp. 75–81.
[4] Duffy, J., Campbell, J. D., and Hawley, R. H., 1971, "On the Use of a Torsional Split Hopkinson Bar to Study Rate Effects in 1100-0 Aluminum," ASME J. Appl. Mech., **38**(1), pp. 83–91.
[5] Nicholas, T., 1973, "An Analysis of the Split Hopkinson Bar Technique for Strain-Rate-Dependent Material Behavior," ASME J. Appl. Mech., **40**(1), pp. 277–282.
[6] Bertholf, L. D., 1974, "Feasibility of Two-Dimensional Numerical Analysis of the Split-Hopkinson Pressure Bar System," ASME J. Appl. Mech., **41**(1), pp. 137–144.
[7] Zhao, H., and Gary, G., 1997, "A New Method for the Separation of Waves: Application to the SHPB Technique for an Unlimited Duration of Measurement," J. Mech. Phys. Solids, **45**(7), pp. 1185–1202.
[8] Chen, W., and Song, B., 2011, *Split Hopkinson (Kolsky) Bar—Design, Testing, and Applications*, Springer: Science+Business Media, LLC, New York.
[9] Shin, H., and Kim, J.-B., 2016, "Understanding the Anomalously Long Duration Time of the Transmitted Pulse From a Soft Specimen in a Kolsky Bar Experiment," Int. J. Precis. Eng. Manuf., **17**(2), pp. 203–208.
[10] Othman, R., 2018, *The Kolsky-Hopkinson Bar Machine*, Springer, Cham.
[11] Kariem, M. A., Santiago, R. C., Govender, R., Shu, D. W., Ruan, D., Nurick, G., Alves, M., Lu, G., and Langdon, G. S., 2019, "Round-Robin Test of Split Hopkinson Pressure Bar," Int. J. Impact Eng., **126**, pp. 62–75.
[12] Shin, H., and Kim, J. B., 2019, "Evolution Specimen Strain Rate in Split Hopkinson Bar Test," Proc. Inst. Mech. Eng. Part C: J. Mech. Eng. Sci., **233**(13), pp. 4667–4687.
[13] Shin, H., and Kim, D., 2020, "One-Dimensional Analyses of Striker Impact on Bar With Different General Impedance," Proc. Inst. Mech. Eng. Part C: J. Mech. Eng. Sci., **234**(2), pp. 589–608.
[14] Samal, M. K., and Sharma, S. A., 2021, "New Procedure to Evaluate Parameters of Johnson–Cook Elastic–Plastic Material Model From Varying Strain Rate Split Hopkinson Pressure Bar Tests," J. Mater. Eng. Perform., **30**, pp. 8500–8514.
[15] Shin, H., Lee, J.-H., Kim, J.-B., and Sohn, S.-I., 2020, "Design Guidelines for the Striker and Transfer Flange of a Split Hopkinson Tension Bar and the Origin of Spurious Waves," Proc. Inst. Mech. Eng. Part C: J. Mech. Eng. Sci., **234**(1), pp. 137–151.
[16] Shin, H., Kim, S., and Kim, J.-B., 2020, "Stress Transfer Mechanism of Flange in Split Hopkinson Tension Bar," Appl. Sci., **10**(21), p. 7601.
[17] Hopkinson, B., 1914, "X. A Method of Measuring the Pressure Produced in the Detonation of High Explosives or by the Impact of Bullets," Philos. Trans. R. Soc. London Ser. A, **213**(497–508), pp. 437–456.
[18] Davies, R. M., 1948, "A Critical Study of the Hopkinson Pressure Bar," Philos. Trans. R. Soc. London Ser. A Math. Phys. Sci., **240**(821), pp. 375–457.
[19] Oliver, J., 1957, "Elastic Wave Dispersion in a Cylindrical Rod by a Wide-Band Short-Duration Pulse Technique," J. Acoust. Soc. Am., **29**(2), pp. 189–194.
[20] Curtis, C. W., 1954, "Second Mode Vibrations of the Pochhammer–Chree Frequency Equation," J. Appl. Phys., **25**(7), p. 928.

[21] Fox, G., and Curtis, C. W., 1958, "Elastic Strain Produced by Sudden Application of Pressure to One End of a Cylindrical Bar. II. Experimental Observations," J. Acoust. Soc. Am., **30**(6), pp. 559–563.
[22] Curtis, C., 1960, "Propagation of an Elastic Pulse in a Semi-Infinite Bar," International Symposium on Stress Wave Propagation in Materials, Pennsylvania State University, June 30–July 3, 1959, pp. 15–43.
[23] Hutchinson, J. R., and Percival, C. M., 1968, "Higher Modes of Longitudinal Wave Propagation in Thin Rod," J. Acoust. Soc. Am., **44**(5), pp. 1204–1210.
[24] Lee, C. K. B., and Crawford, R. C., 1993, "A New Method for Analysing Dispersed Bar Gauge Data," Meas. Sci. Technol., **4**(9), pp. 931–937.
[25] Lee, C. K. B., Crawford, R. C., Mann, K. A., Coleman, P., and Petersen, C., 1995, "Evidence of Higher Pochhammer–Chree Modes in an Unsplit Hopkinson Bar," Meas. Sci. Technol., **6**(7), pp. 853–859.
[26] Yew, E. H., and Chen, C. S., 1978, "Experimental Study of Dispersive Waves in Beam and Rod Using FFT," ASME J. Appl. Mech., **45**(4), pp. 940–942.
[27] Tyas, A., and Ozdemir, Z., 2014, "On Backward Dispersion Correction of Hopkinson Pressure Bar Signals," Philos. Trans. R. Soc. A Math. Phys. Eng. Sci., **372**, p. 20130291.
[28] Barr, A. D., Rigby, S. E., and Clayton, M., 2020, "Correction of Higher Mode Pochhammer–Chree Dispersion in Experimental Blast Loading Measurements," Int. J. Impact Eng., **139**, p. 103526.
[29] Yang, J., He, J., Zhang, D., Xu, H., Shi, G., Zhang, M., Liu, W., and Zhang, Y., 2020, "Local Phase-Amplitude Joint Correction for Free Surface Velocity of Hopkinson Pressure Bar," Appl. Sci., **10**(15), p. 5390.
[30] Rigby, S. E., Clayton, M., and Barr, A. D., 2018, "A Review of Pochhammer–Chree Dispersion in the Hopkinson Bar," Proc. Inst. Civil. Eng.—Eng. Comput. Mech., **171**(1), pp. 3–13.
[31] Pavlakovic, B., Lowe, M., and Cawley, P., 2001, "High-Frequency Low-Loss Ultrasonic Modes in Imbedded Bars," ASME J. Appl. Mech., **68**(1), pp. 67–75.
[32] Love, A. E. H., 1944, *A Treatise on the Mathematical Theory of Elasticity*, 4th ed., Reprinted, Dover Publications, New York.
[33] Pochhammer, L., 1876, "Über Fortplanzungsgeschwindigkeiten Kleiner Schwingungen in Einem Unbergrenzten Isotropen Kreiszylinder (On the Propagation Velocities of Small Oscillations in an Unlimited Isotropic Circular Cylinder)," Zeitschrift für Reine und Angewandte Mathematik Z. Reine Angew Math., **81**, pp. 324–336.
[34] Chree, C., 1886, "Longitudinal Vibrations of a Circular Bar," Q. J. Pure Appl. Math., **21**, pp. 287–298.
[35] Chree, C., 1889, "The Equations of an Isotropic Elastic Solid in Polar and Cylindrical Coordinates, Their Solutions and Applications," Trans. Cambridge Philos. Soc., **14**, pp. 251–369.
[36] Bancroft, D., 1941, "The Velocity of Longitudinal Wave in Cylindrical Bars," Phys. Rev., **59**(7), pp. 588–593.
[37] Shin, H., 2022, "Pochhammer–Chree Equation Solver for Dispersion Correction of Elastic Waves in a (Split) Hopkinson Bar," Proc. Inst. Mech. Eng. Part C: J. Mech. Eng. Sci., **236**(1), pp. 80–87.
[38] Shin, H., 2022, "Pochhammer–Chree Equation Solver for Dispersion Correction of Elastic Waves in a (Split) Hopkinson Bar – A Revised Version," ResearchGate
[39] Brizard, D., 2020, "An Impact Test to Determine the Wave Speed in SHPB: Measurement and Uncertainty," J. Dyn. Behav. Mater, **6**(1), pp. 45–52.
[40] Shin, H., 2022, "Manual for Calibrating Sound Speed and Poisson's Ratio of (Split) Hopkinson Bar via Dispersion Correction Using Excel® and Matlab® Templates." Submitted to Data.
[41] Shin, H., 2022, "Templates for Calibrating Sound Speed and Poisson's Ratio of (Split) Hopkinson Bar via Dispersion Correction of Elastic Wave," ResearchGate.
[42] Lee, J.-H., Shin, H., Kim, J.-B., Kim, J.-Y., Park, S.-T., Kim, G.-L., and Oh, K.-W., 2019, "Determination of the Flow Stress–Strain Curve of Aluminum Alloy and Tantalum Using the Compressive Load–Displacement Curve of a Hat-Type Specimen," ASME J. Appl. Mech., **86**(3), p. 031012.
[43] Shin, H., Lee, J.-H., Kim, J.-B., Seo, S.-J., Lee, J.-K., Lee, J.-O., Yoon, T.-S., and Jeong, C.-S., 2019, "Numerical Verification of the Schroeder–Webster Surface Types and Friction Compensation Models for a Metallic Specimen in Axisymmetric Compression Test," ASME J. Tribol., **141**(10), p. 101401.
[44] Lee, J.-H., Shin, H., Seo, S.-J., Lee, J.-K., Lee, J.-O., Yoon, T.-S., and Jung, C.-S., 2019, "A Design of a Phenomenological Friction-Compensation Model via Numerical Experiment for the Compressive Flow Stress–Strain Curve of Copper (in Korean)," Kor. J. Comput. Des. Eng., **24**(1), pp. 1–9.
[45] Johnson, G. R., and Cook, W. H., 1983, "A Constitutive Model and Data for Metals Subjected to Large Strains, High Strain Rates and High Temperatures," Proceedings of 7th International Symposium of Ballistics, The Hague, Netherlands, Apr. 19–21, pp. 541–547.
[46] Shin, H., and Kim, J.-B., 2010, "A Phenomenological Constitutive Equation to Describe Various Flow Stress Behaviors of Materials in Wide Strain Rate and Temperature Regimes," ASME J. Eng. Mater. Technol., **132**(2), p. 021009.
[47] Yoo, Y.-H., Paik, S.-H., Kim, J.-B., and Shin, H., 2013, "Performance of a Flying Cross Bar to Incapacitate a Long-Rod Penetrator Based on a Finite Element Model," Eng. Comput., **29**(4), pp. 409–415.
[48] Yoo, Y.-H., Paik, S.-H., Kim, J.-B., and Shin, H., 2013, "Effects of Impact Location and Angle of a Flying Cross Bar on the Protection of a Long-Rod Penetrator," Trans. Can. Soc. Mech. Eng., **37**(4), pp. 1115–1125.
[49] Kim, D., Lee, J.-H., Shin, H., Kim, J.-Y., Park, S.-T., Song, Y.-H., and Oh, K. W., 2019, "A Numerical Study on the Influence of the Flow Stress of Copper Liner on the Penetration Performance of a Small-Caliber High Explosive (in Korean)," Kor. J. Comput. Des. Eng., **24**(3), pp. 300–310.
[50] Shin, H., and Yoo, Y.-H., 2003, "Effect of the Velocity of a Single Flying Plate on the Protection Capability Against Obliquely Impacting Long-Rod Penetrators," Combust. Explos. Shock Waves, **39**(5), pp. 591–600.
[51] Yoo, Y.-H., and Shin, H., 2004, "Protection Capability of Dual Flying Plates Against Obliquely Impacting Long-Rod Penetrators," Int. J. Impact Eng., **30**(1), pp. 55–68.
[52] Lee, W., Lee, H.-J., and Shin, H., 2002, "Ricochet of a Tungsten Heavy Alloy Long-Rod Projectile From Deformable Steel Plates," J. Phys. D: Appl. Phys., **35**(20), pp. 2676–2686.
[53] Kim, D., Shin, H., Jung, D., Lee, E., Seo, S., and Yoon, T.-S., 2019, "A Numerical Study on Jet Formation and Penetration Characteristics of the Shaped Charge With an Aspect Ratio of 2.73 and a High-Strength Copper Liner (in Korean)," Kor. J. Comput. Des. Eng., **24**(1), pp. 73–83.
[54] Shin, H., Lee, H.-J., Yoo, Y.-H., and Lee, W., 2004, "A Determination Procedure for Element Elimination Criterion in Finite Element Analysis of High-Strain-Rate Impact/Penetration Phenomena," JSME Int. J. Ser. A Solid Mech. Mater. Eng., **47**(1), pp. 35–41.
[55] Gorham, D. A., 1983, "A Numerical Method for the Correction of Dispersion in Pressure Bar Signals," J. Phys. E Sci. Instum., **16**(6), pp. 477–479.
[56] Follansbee, P. S., and Frantz, C., 1983, "Wave Propagation in the Split Hopkinson Pressure Bar," ASME J. Eng. Mater. Technol., **105**(1), pp. 61–66.
[57] Felice, C. W., 1986, "The Response of Soil to Impulse Loads Using the Split Hopkinson Pressure Bar Technique," AFWL-TR-85-92, Final Report, Air Force Weapons Lab, Kirtland Air Force Base, NM.
[58] Gong, J. C., Malvern, L. E., and Jenkins, D. A., 1990, "Dispersion Investigation in the Split Hopkinson Pressure Bar," ASME J. Eng. Mater. Technol., **112**(3), pp. 309–314.
[59] Lifshitz, J. M., and Leber, H., 1994, "Data Processing in the Split Hopkinson Pressure Bar Tests," Int. J. Impact Eng., **15**(6), pp. 723–733.
[60] Li, Z., and Lambros, J., 1999, "Determination of the Dynamic Response of Brittle Composites by the Use of the Split Hopkinson Pressure Bar," Compos. Sci. Technol., **59**(7), pp. 1097–1107.
[61] Marais, S. T., Tait, R. B., Cloete, T. J., and Nurick, G. N., 2004, "Material Testing at High Strain Rate Using the Split Hopkinson Pressure Bar," Latin Am. J. Solids Struct., **1**(3), pp. 319–334. https://www.lajss.org/index.php/LAJSS/article/view/53
[62] Gama, B. A., Lopatnikov, S. L., and Gillespie, J. W., 2004, "Hopkinson Bar Experimental Technique: A Critical Review," ASME Appl. Mech. Rev., **57**(4), pp. 223–250.
[63] Merle, R., and Zhao, H., 2006, "On the Errors Associated With the Use of Large Diameter SHPB, Correction for Radially Non-Uniform Distribution of Stress and Particle Velocity in SHPB Testing," Int. J. Impact Eng., **32**(12), pp. 1964–1980.
[64] Luo, H. H., Tan, Z. H., Han, X., and Chen, C., 2012, "An Investigation on Dynamic Properties of Aluminium Alloy Foam Using Modified Large Scale SHPB Based on Dispersion Correction," Comput. Mater. Continua, **12**(1), pp. 1–13.
[65] Wang, Z., and Li, P., 2015, "Characterisation of Dynamic Behaviour of Alumina Ceramics: Evaluation of Stress Uniformity," AIP Adv., **5**(10), p. 107224.
[66] Bragov, A. M., Lomunov, A. K., Lamzin, D. A., and Konstantinov, K. Y., 2019, "Dispersion Correction in Split-Hopkinson Pressure Bar: Theoretical and Experimental Analysis," Continuum Mech. Thermodyn.
[67] Rayleigh, J. W. S., 1975, *The Theory of Sound*, Vols. I and II. Dover Publications, New York.
[68] Meijers, P. C., Tsouvalas, A., and Metrikine, A. V., 2017, "The Effect of Stress Wave Dispersion on the Drivability Analysis of Large-Diameter Monopiles," Procedia Eng., **199**, pp. 2390–2395.
[69] Yang, H., Li, Y., and Zhou, F., 2021, "Propagation of Stress Pulses in a Rayleigh-Love Elastic rod," Int. J. Impact Eng., **153**, p. 103854. .
[70] Kolsky, H., 1953, *Stress Waves in Solids*, Clarendon Press, Oxford, p. 61.
[71] Graff, K. F., 1975, *Wave Motion in Elastic Solids*, Clarendon Press, Oxford, p. 120.
[72] Hsieh, D. Y., and Kolsky, H., 1958, "An Experimental Study of Pulse Propagation in Elastic Cylinder," Proc. Phys. Soc., **71**(4), pp. 608–612.
[73] MathWorks®, https://mathworks.com/help/matlab/ref/fminsearch.html, Accessed March 24, 2022.
[74] ASTM B962-17, 2017, *Standard Test Methods for Density of Compacted or Sintered Powder Metallurgy (PM) Products Using Archimedes' Principle*, ASTM International, West Conshohocken, PA.
[75] ASTM D792-20, 2020, *Standard Test Methods for Density and Specific Gravity (Relative Density) of Plastics by Displacement*, ASTM International, West Conshohocken, PA.
[76] ASTM D854-14, 2014, *Standard Test Methods for Specific Gravity of Soil Solids by Water Pycnometer*, ASTM International, West Conshohocken, PA.
[77] Dharan, C. K. H., and Hauser, F. E., 1970, "Determination of Stress-Strain Characteristics at Very High Strain Rates," Exp. Mech., **10**(9), pp. 370–376.
[78] Malinowski, J. Z., Klepaczko, J. R., and Kowalewski, Z. L., 2007, "Miniaturized Compression Test at Very High Strain Rates by Direct Impact," Exp. Mech., **47**(4), pp. 451–463.
[79] Couque, H., 2014, "The Use of the Direct Impact Hopkinson Pressure Bar Technique to Describe Thermally Activated and Viscous Regimes of Metallic Materials," Philos. Trans. R. Soc. A Math. Phys. Eng. Sci., **372**, p. 20130218.
[80] Basalin, A., Konstantinov, A., Igumnov, L., Belov, A., Bragov, A., and Eremeyev, Victor, 2022, "The Direct Impact Method for Studying Dynamic Behavior of Viscoplastic Materials," J. Appl. Comput. Mech., **8**(2), pp. 597–604.
[81] Jang, T. J., Kim, J., and Shin, H., 2021, "Plastic Constitutive Johnson–Cook Model Parameters by Optimization-Based Inverse Method," J. Comput. Design Eng., **8**(4), pp. 1082–1097.